Surface & Coatings Technology 525 (2026) 133312

Contents lists available at ScienceDirect

Surface & Coatings Technology

journal homepage: www.elsevier.com/locate/surfcoat

Preparation of TaZrHfNbTi high-entropy coating with a gradient nanocomposite structure and its melting-loss behavior in dynamic molten aluminum

Dongbo Wei [a,b,*], Zuoxin Mao [a,b], Muyao Lin [a,b], Pingze Zhang [a,b], Wenping Liang [a,b], Zhengjun Yao [a,b], Zhenyu Wang [c], Aiying Wang [c]

[a] College of Materials Science and Technology, Nanjing University of Aeronautics and Astronautics, Nanjing, 211106, China
[b] Materials Preparation and Protection for Harsh Environment Key Laboratory of Ministry of Industry and Information Technology, Nanjing, 211106, China
[c] Key Laboratory of Advanced Marine Materials, Ningbo Institute of Materials Technology and Engineering, Chinese Academy of Sciences, Ningbo, 315201, China

ARTICLE INFO

Keywords:
Non-equilibrium sputtering deposition
Refractory high-entropy alloy coating
Nanocomposite structure
Diffusion interface bonding
Corrosion of molten aluminum

ABSTRACT

A protective TaZrHfNbTi high-entropy alloy (HEA) coating was prepared on the surface of H13 steel by hollow cathode discharge-enhanced plasma sputtering deposition. The microstructure, phase composition, microscopic mechanical properties, and melting-loss behavior of the coating in dynamic molten aluminum were investigated. Under the influence of hollow cathode discharge-enhanced nonequilibrium sputtering, the coating exhibited a gradient nanostructure and formed a diffusion bond with the substrate. From the surface to the interior, the coating consisted of three different zones: a nanocomposite structure zone of "nanocrystalline + amorphous" in the outmost layer, a nanostructured columnar crystal zone in the intermediate layer, and a diffusion interface zone between the coating and the substrate. The TaZrHfNbTi coating with a diffusion interface and gradient nanostructure showed good resistance to melting loss in dynamic molten aluminum and did not peel off after 6 h of exposure to dynamic molten aluminum at 680 °C. The degradation mechanism of the coating was mainly attributed to the gradual degradation of the body-centered cubic (BCC) structure under high-temperature molten aluminum, during which each element in the coating either oxidized or formed intermetallic compounds, depending on its affinity with O and Al. Ti and Zr in the coating were oxidized to form Ti_2O and ZrO_2. Al_3Ti and Al_2Ta formed due to the high affinity of Ti and Ta with Al, while the remaining Hf and Nb combined into HfNb.

1. Introduction

High-entropy alloys (HEAs) are alloys prepared from five or more metals with equal or approximately equal amounts of substance. Through reasonable composition design and structural regulation, HEAs can be endowed with multiple characteristics including high hardness, high wear resistance, and high thermal/chemical stability, thus providing new scientific insights and broad research space for exploring protective coating material systems serving in multi-factor coupling environments (high temperature and high pressure, friction and wear, strong dielectric corrosion, erosion and ablation, space irradiation, etc.) [1,2]. However, these characteristics also pose new challenges for the microstructure design of HEA coatings. The common problem lies in how to overcome the large differences in composition and physical properties (hardness, toughness, thermal expansion coefficient, etc.) between the HEA coating and the substrate metal, and how to improve the bonding strength between the coating and the substrate. In particular, solving this problem is important for improving the reliability and service life of HEA coatings in the above multi-factor coupling harsh environments. Unfortunately, existing preparation methods for HEA coatings all seem to encounter this problem. For example, as the main technical means of preparing HEA coatings, magnetron sputtering can generally produce films or coatings with compact structures and high hardness, but the films or coatings lack a good transition zone with the substrate, so the bonding strength is greatly limited. In the face of multi-factor coupling harsh environments, the films or coatings easily peel off, leading to early failure. For example, Deng et al. [3] fabricated CoCrFeNiMo high-entropy alloy coatings using high-velocity oxygen fuel spraying and high-frequency induction remelting, and found that Fe/Mo interdiffusion at the coating-steel substrate interface led to the

* Corresponding author at: College of Materials Science and Technology, Nanjing University of Aeronautics and Astronautics, Nanjing, 211106, China.
E-mail address: weidongbo@nuaa.edu.cn (D. Wei).

https://doi.org/10.1016/j.surfcoat.2026.133312
Received 8 January 2026; Received in revised form 13 February 2026; Accepted 17 February 2026
Available online 17 February 2026

formation of $Fe_{63}Mo_{37}$ R-phase, which constitutes the primary interfacial defect. Zhang et al. [4] fabricated an AlCoCrFeNi high-entropy alloy bond coating using vacuum plasma spraying followed by vacuum heat treatment, and noted that the primary interfacial defect stems from the higher grain boundary density in the as-sprayed coating, which promotes outward diffusion of Al ions and leads to thickening of the thermally grown oxide layer. So far, preparation techniques for HEA films or coatings based on sputtering methods have all encountered the problem of interface transition. On the other hand, although a metallurgical transition interface can be formed by using surface metallurgy to prepare HEA coatings, it often requires high temperatures during the preparation process, which may cause remelting of the substrate surface layer, thus adversely affecting substrate properties and bringing challenges to fine microstructure regulation. For example, in the laser cladding process, pore defects and abnormal microstructure coarsening may occur in the prepared HEA cladding layer [5].

Hollow cathode discharge is a special form of glow discharge, which has the characteristics of high current density typical of abnormal glow discharge. Due to the hollow cathode discharge effect, the peak electron density in the steady state can reach 5×10^{14} cm^{-3}, facilitating the generation of high-density plasma. When this effect is applied to glow discharge sputtering deposition, a higher ionization rate of the target metal and a higher deposition temperature can be achieved. In this study, a non-equilibrium sputtering deposition field was constructed based on the plasma hollow cathode discharge-enhanced sputtering deposition. A target electrode (TE) and a substrate electrode (SE) were mounted in a vacuum chamber (anode). The anode and TE were connected to pulsed DC power supplies, whereas the anode and the SE were connected to DC power supplies. The potential difference between the substrate and the target resulted in an unequal electronic potential hollow cathode effect. Once heated to a given temperature, the ions or atoms sputtered from the target were deposited on the substrate because of the negative bias lower than that of the target. The ions and atoms diffused into the substrate when the temperature was elevated, leading to the development of a coating on the substrate. More importantly, this technique used the substrate and the HEA target as two cathodes to construct an electric field that can produce the hollow cathode effect between them, and employed the electric field energy for non-equilibrium sputtering to improve the ionization rate [6–8]. Its outstanding feature is that the substrate surface is sputtered while the target is sputtered, which can produce many vacancies in the surface layer of the substrate, thus endowing the substrate surface with higher activity. When the atomic groups of the target components are deposited on the surface of the substrate, they can gain enough energy to diffuse from the surface to the interior, thus forming a coating with a certain thickness of diffusion interface [9,10]. Fig. 1 illustrates the principle of the plasma surface coating technique enhanced by the hollow cathode discharge effect in this study.

Over the past decade, integrated die casting technology developed by Tesla has been widely used in the automotive industry. This technology offers the advantages of light weight, reduced manufacturing cost, and improved structural strength. However, integrated die casting requires a molding temperature of 700 °C and an injection speed of 20–60 m/s. This harsh working environment leads to frequent maintenance and replacement of die-casting molds and makes their surface protection an urgent task [1,2,11]. As mentioned above, HEA materials provide a new material system to address this problem.

In recent years, there has been extensive discussion and research on the protection provided by HEAs against molten salt or molten metal. Xie et al. [12] prepared FeCrNiMoAl HEA coatings by the laser cladding method and found that the corrosion rate in a mixture of molten salts such as NaCl and KCl at 600 °C was 34% lower than that of traditional Inconel 625. Garip et al. [13] prepared $Fe_2CoCrNi_{0.5}$-based HEAs by combining powder metallurgy with electrical current-assisted sintering (ECAS) and investigated their hot corrosion behavior in NaCl molten salt, finding that the addition of Si contributed to improved corrosion resistance. Gong et al. [14] prepared an $Al_{0.4}CoCrFeNi$ HEA by vacuum induction melting and studied its corrosion resistance in liquid lead-bismuth eutectic, finding that deterioration of corrosion resistance was attributed to interphase boundary (IB) wetting generated by BCC/FCC IBs. Yang et al. [15] designed and prepared $Ti_{40}Nb_{25}Cr_{15}Mo_{10}Al_{10}$ and $Ti_{40}Nb_{20}Cr_{20}Mo_{10}Al_{10}$ refractory high-entropy alloys (RHEAs) and found that the low solubility of constituent elements in molten aluminum and the slow diffusion of Al atoms in the RHEA substrate were responsible for the excellent corrosion resistance of the RHEAs.

In summary, while numerous studies have examined the corrosion behavior of high-entropy alloy coatings in molten metals or molten salts, most focus on static corrosion conditions. Furthermore, research on dynamic corrosion behavior remains limited, and existing studies in this area generally do not fall within the scope of high-entropy alloy coatings [16,17]. Ta, Zr, Hf, Nb, and Ti are refractory metal elements with high melting points. The body-centered cubic solid solution formed by these five elements retains structural stability at elevated temperatures, endowing the resulting high-entropy alloy with high-temperature strength and corrosion resistance [18–20]. Consequently, the TaZrHfNbTi high-entropy alloy coating holds promising application value and merits further investigation under harsh dynamic molten aluminum corrosion conditions.

Herein, the hollow cathode discharge-enhanced plasma surface diffusion coating technique was employed to prepare a protective coating of TaZrHfNbTi HEA on the surface of H13 steel, and the composition, microstructure, phase structure, and melting loss behavior in dynamic molten aluminum of the coating were investigated.

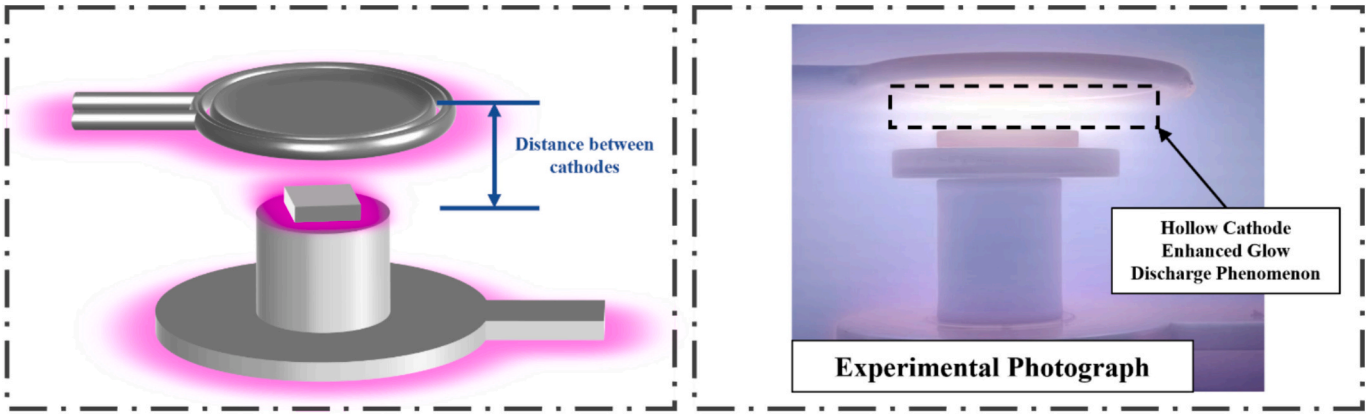

Fig. 1. Schematic diagram of hollow cathode discharge-enhanced plasma sputtering deposition.

2. Experimental

2.1. Substrate pretreatment and coating deposition

H13 steel was selected as the substrate material and machined into square samples with dimensions of 15 mm × 15 mm × 5 mm by wire cutting. The samples were then successively ground, polished, and ultrasonically cleaned. The grinding process was carried out using metallographic sandpapers from grades 01# to 07#. A bright surface was obtained after polishing. For ultrasonic cleaning, the samples were immersed in anhydrous ethanol for 15 min to remove fine contaminants from the surface. The refractory high-entropy target was composed of five elements—Ta, Zr, Hf, Nb, and Ti—in equiatomic ratio. It was prepared by vacuum melting using metals with purity ≥ 99.95%, and then processed into a flat cylindrical shape with a diameter of 100 mm and a thickness of 5 mm.

A TaZrHfNbTi refractory high-entropy coating was deposited onto the H13 steel surface via sputtering based on the hollow cathode discharge effect. Ionized Ar formed high-energy-density Ar^+ ions, which were accelerated by an electric field to bombard both the negatively biased high-entropy target and the steel sample. Under bombardment, metal particles were sputtered from the target and deposited onto the surface of the H13 sample. Simultaneously, bombardment of the H13 substrate raised its temperature and created a vacancy concentration gradient on the surface due to particle impact, which promoted the inward diffusion of the deposited metal particles. As a result, a high-entropy alloy coating with a discernible diffusion interface was formed. The process parameters used in this study are listed in Table 1.

2.2. Microstructural characterization

The microstructural morphology of the H13 steel and the TaZrHfNbTi coating before and after testing was examined using a Scios 2 HiVac focused ion beam–scanning electron microscope (SEM). The SEM was operated at an acceleration voltage of 20 kV with a resolution of less than 5 nm. Quantitative compositional analysis of the sample surface was performed using an integrated energy-dispersive X-ray spectroscopy (EDS) system. The surface three-dimensional topography of the H13 steel and the TaZrHfNbTi coating after melting loss behavior testing was acquired with an OLS5100 atomic force microscope (AFM). The data of corrosion pit area ratio in the three-dimensional surface morphology of the H13 steel and the TaZrHfNbTi coating were quantified by ImageJ software [21]. The phase structure of the TaZrHfNbTi coating before and after testing was characterized using an Empyrean X-ray diffractometer (XRD). XRD measurements were conducted with Cu-Kα radiation (λ = 0.15418 nm) under operating conditions of 45 kV and 40 mA. The scanning range was 10°–90° with a step size of 0.01313° and a scanning rate of 10°/min. To observe the coating cross-section at the nanoscale, samples were prepared using a Scios 2 HiVac focused ion beam (FIB) system. Cross-sectional imaging was then carried out on a Talos F200X G2 field-emission high-resolution transmission electron microscope (TEM) at an acceleration voltage of 200 kV. The resolutions of the TEM and scanning TEM (STEM) modes were 0.25 nm and 0.16 nm, respectively.

Table 1
Process parameters of TaZrHfNbTi coating.

Items	Parameters
Working pressure (Pa)	45
Cathode distance (mm)	20
Target electrode (V)	1000
Substrate electrode (V)	450
Deposition time (h)	5

2.3. Micromechanical properties

Samples were tested using an HVS-1000 micro-hardness tester under a load of 50 g. Nanoindentation measurements were performed with a Bruker/TI 980 nano indenter equipped with a triangular pyramid diamond tip. The tests were conducted under a maximum load of 50 mN, a loading rate of 5 mN/s, and a dwell time of 10 s. The elastic deformation work (W_e) represents the energy stored in the material during elastic deformation, i.e., the elastic potential energy. The plastic deformation work (W_p) corresponds to the work done by external forces during plastic deformation. Both W_e and W_p can be calculated from the areas enclosed by the loading curve, holding curve, unloading curve, and the indentation depth axis.

2.4. Melting loss behavior testing

The melting loss test of the samples was a dynamic corrosion process. Dynamic corrosion refers to immersing the samples in molten aluminum and stirring the melt to simulate the working condition of high-velocity aluminum liquid scouring the sample surface. During the melting loss experiment, the stirrer rotation speed was set to 600 r/min, and the molten aluminum temperature was set to 680 °C. At 680 °C, the substrate samples and coated samples were subjected to corrosion for 15 min, 40 min, 2 h, and 6 h, respectively. The test equipment was independently designed and assembled, as shown in Fig. 2.

The melting loss mechanisms of the H13 steel and the TaZrHfNbTi coating were analyzed based on the post-corrosion microstructure and corrosion products. The resistance of the TaZrHfNbTi coating to molten aluminum melting loss was verified by calculating the corrosion rate. Prior to testing, the samples were polished to reduce their surface roughness, facilitating a clearer comparison of melting loss morphologies under different parameters. Polishing was performed using a combination of cashmere polishing cloth and a 0.25 μm polishing compound. Polishing times of 30 s and 15 s were set for the H13 steel and TaZrHfNbTi coated samples, respectively, ensuring a flat microscopic surface morphology.

3. Results

3.1. Composition, microstructure, and phase structure of the coating

Fig. 3 shows the surface microscopic morphology and elemental distribution of the TaZrHfNbTi coating. The alloy coating exhibits a compact surface microstructure with uniform distribution of constituent elements. Under the influence of hollow cathode sputtering and high-energy particle bombardment, the coating presents a trend of aggregating growth with metal particles in micro-zones as nuclei, showing a characteristic “island bulge” morphology. EDS scanning analysis shows that the atomic percentages of Ta, Zr, Hf, Nb, and Ti elements in the coating surface layer are 25.64%, 15.51%, 12.19%, 22.95% and 23.71 at.%, respectively. The different sputtering rates of different elements under non-equilibrium sputtering lead to some deviations between the coating and the target compositions, which is mainly attributed to the different sputtering rates of HEA elements under Ar^+ bombardment. The area-scanning results, as shown in Fig. 3(b–f), show that all elements are uniformly distributed in the coating surface layer without obvious segregation.

Fig. 4 shows the cross-sectional microscopic morphology and corresponding elemental distribution of the TaZrHfNbTi coating. Fig. 4(a) shows that the coating is approximately 19 μm in thickness and has a compact structure without defects. Fig. 4(b) shows that the coating can be divided into two zones based on the distribution characteristics of elements. In the 5–7 μm zone, Fe in the substrate shows a gradient decrease, while the high-entropy component elements in the coating show a gradient increase, indicating the formation of a gradient transition interface between the coating and the substrate. In the 7–24 μm

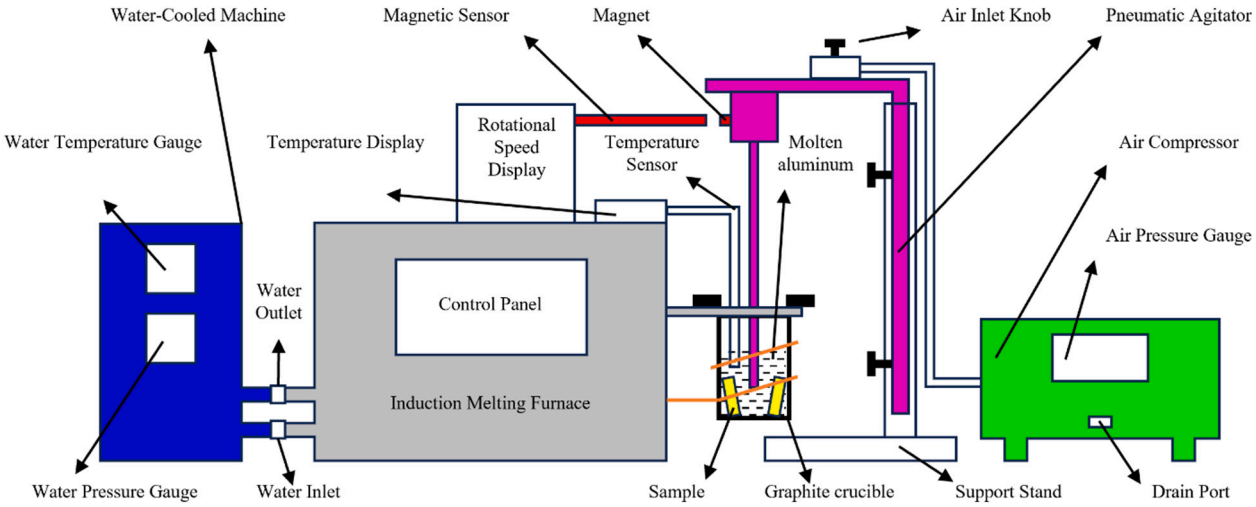

Fig. 2. Schematic diagram of dynamic molten aluminum test.

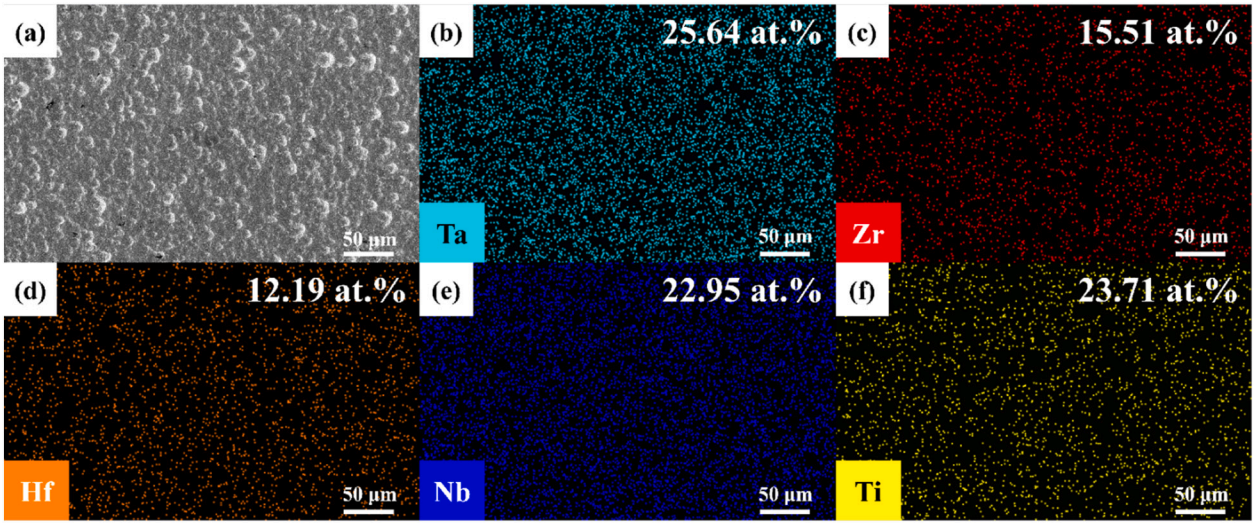

Fig. 3. Surface microscopic morphology and composition of TaZrHfNbTi coating. (a) Secondary electron image of TaZrHfNbTi coating surface. (b–f) Elemental distribution and contents of TaZrHfNbTi coating surface.

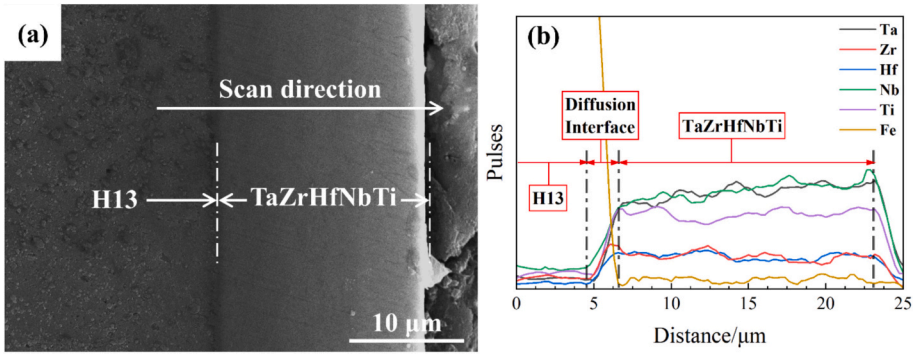

Fig. 4. Cross-sectional microscopic morphology and corresponding elemental distribution of the TaZrHfNbTi coating. (a) Secondary electron cross-section image of the coating. (b) Linear scanning distribution of elements in the coating.

zone, there are mainly high-entropy component elements, which are deposited on the surface of the die-steel sample after sputtering the HEA target.

Fig. 5 presents the XRD pattern of the TaZrHfNbTi coating, which shows extremely strong diffraction peaks corresponding to a BCC structure [22–24]. This indicates that the main phase of the coating is a BCC solid solution. Moreover, the diffraction intensity corresponding to the (110) crystal plane in the BCC structure shows an extremely strong

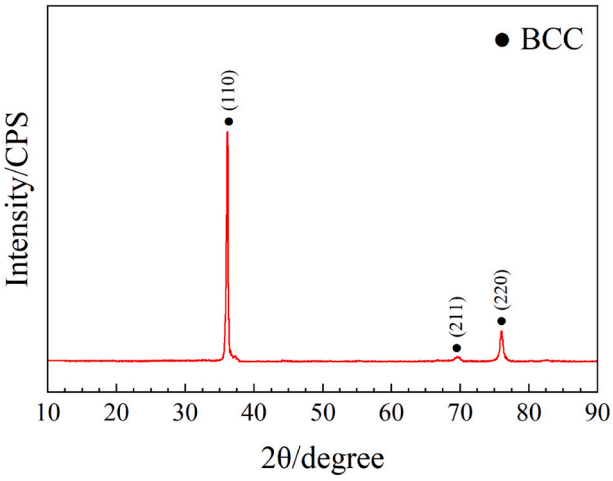

Fig. 5. XRD pattern of TaZrHfNbTi coating.

intensity, indicating preferential growth in this direction. TEM characterization of the coated sample along the cross-sectional growth direction of the coating, as shown in Figs. 6–8, demonstrates that there are abundant nanophases in the coating, forming a complex nanocomposite structure and showing significant gradient changes in the depth direction.

Fig. 6 shows the nanocomposite structure and phase composition in the surface layer of the coating. As can be seen from Fig. 6(a), the surface layer is composed of a large number of nano-precipitated phases. The selected area electron diffraction (SAED) pattern reveals that the phase composition in the surface layer consists of BCC solid solution and an amorphous phase. Compared with other crystal planes, the (110) crystal plane in the BCC solid solution exhibits a diffraction ring with extremely high intensity, which is consistent with the XRD pattern. The Fourier transform calibration pattern shows a crystal-plane spacing of 0.23 nm for the (110) plane, and the corresponding atomic arrangement structure is visible by high-resolution observation, as shown in region C in Fig. 6 (b). It is worth noting that a certain proportion of spherical amorphous nano-precipitated phases appear in the surface layer, as shown in region B of Fig. 6(b). Therefore, the phase structure of the coating surface layer can be summarized as a BCC solid solution with diffusely distributed spherical amorphous precipitated phases.

With increasing depth, the microstructure of the coating transforms into nanostructured columnar crystals distributed along the growth direction, and numerous nano-precipitated phases can be observed in both the interior and boundary regions of the columnar crystals, as shown in Fig. 7(a). It is worth noting that the coating in this intermediate layer contains a certain amount of Fe. This is because the hollow cathode discharge effect induces strong counter-sputtering on the substrate surface at the initial stage of deposition. As a result, a certain amount of Fe is sputtered out and deposited into the coating along with the alloying elements during subsequent deposition. In particular, the addition of Fe induces noticeable changes in the phase structure of the coating. Inside the columnar crystals, the Fe content is high, promoting the precipitation of nanocrystalline phases with BCC structure and a large number of fine nano-amorphous phases, as shown in region B of Fig. 7(a). However, the Fe content at the junction regions of the columnar crystals is low, resulting in Fe-depleted amorphous regions, where fine nano-sized precipitated phases with FCC structure and nano-sized precipitated phases with BCC structure appear, as shown in region A of Fig. 7(a). These results indicate that the addition of Fe induces the formation of nano-sized precipitated phases in the columnar-crystal zone, with the types closely related to the Fe content. Fig. 7(b2) shows that the (111) crystal-plane spacing in the FCC solid-solution structure is about 0.258 nm. The HAADF-STEM image and corresponding EDS map in Fig. 7(d) show that the alloying elements are evenly distributed overall, but Fe exhibits obvious segregation. In summary, the intermediate layer of the coating is mainly composed of columnar nanocrystals. Nanocrystalline phases with BCC structure and fine spherical nano-sized amorphous phases exist in the interior of the columnar nanocrystals, while nanocrystalline phases with BCC and FCC solid-solution structure precipitate in the amorphous regions at the boundaries of the columnar nanocrystals.

Fig. 8 shows the microscopic morphology and element diffusion at the coating/matrix diffusion interface. The TEM image in Fig. 8(a) shows that the diffusion interface between the coating and substrate presents the characteristic of a gradient multilayered nanostructure. In this diffusion interface zone, the dispersively distributed nanocrystalline and nano-sized amorphous phases gradually separate with increasing depth toward the substrate, as shown in Fig. 8(b1), (c1), and (d1). Nanocrystalline grains with BCC structure aggregate to form a large number of nano-sized precipitated crystal phases and stacking faults in region b1, but amorphous phases are not observed, as shown in Fig. 8 (b1) and (b2). Similarly, no crystal precipitates are observed in region d1 of the amorphous region, as shown in Fig. 8(d1) and (d2). The c1 region between these two regions consists of a mixture of crystal and amorphous phases, as shown in Fig. 8(c1) and (c2). The HAADF-STEM image and corresponding EDS element distribution show that Fe diffuses gradiently from the substrate into the coating, whereas the HEA elements gradually diffuse toward the substrate, as shown in Fig. 8(e). It can be concluded that these phenomena are induced by the outward diffusion of Fe at the coating/substrate interface. The introduction of Fe into the

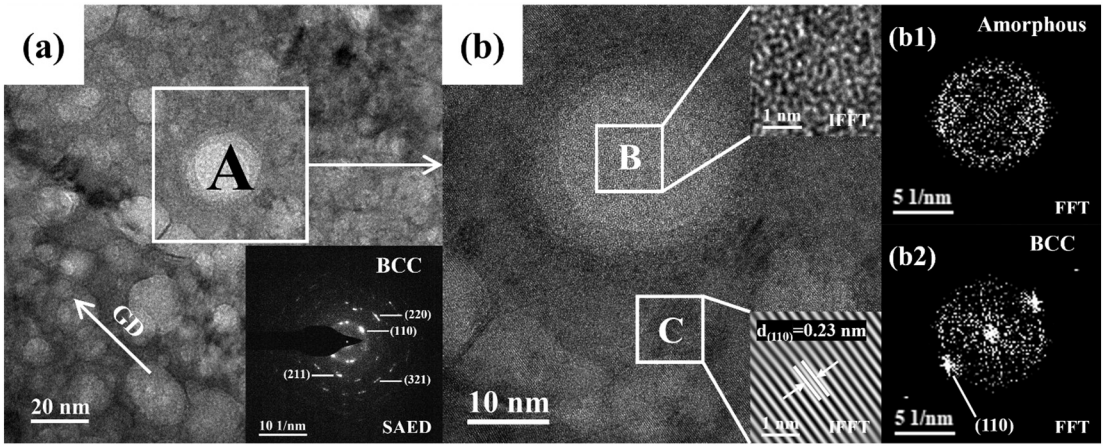

Fig. 6. Nanocomposite structure of the coating surface layer. (a) is bright-field image of the coating surface layer with SAED pattern inset. (b) is the local high-resolution bright-field image of the designated area A in (a). (b1) is the corresponding FFT pattern of area B. (b2) is the corresponding FFT pattern of area C.

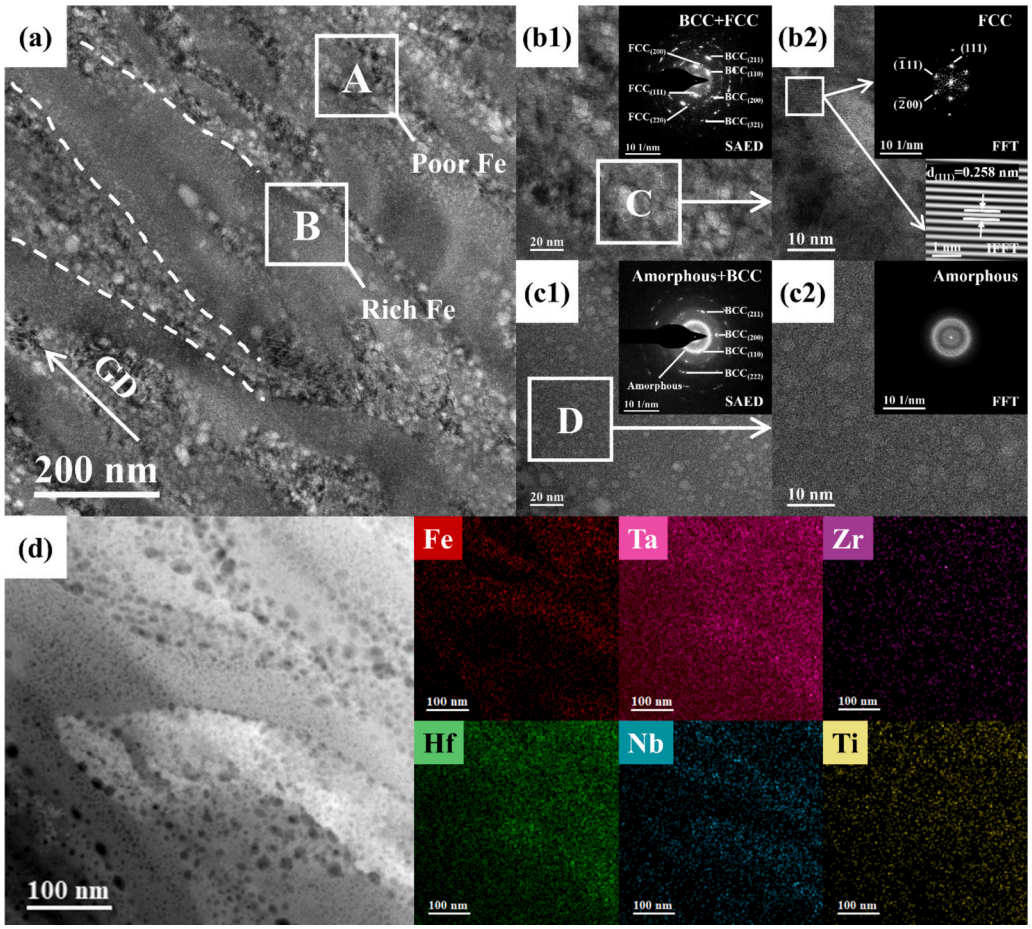

Fig. 7. Nanocomposite structure of the coating intermediate layer. (a) is bright-field image of the coating intermediate layer. (b1) is the local high-resolution bright-field image of the designated area A in (a) with SAED pattern inset. (c1) is the local high-resolution bright-field image of the designated area B in (a) with SAED pattern inset. (b2) is the local high-resolution bright-field image of the designated area C in (b1). (c2) is the local high-resolution bright-field image of the designated area D in (c1). (d) HAADF-STEM image of the coating intermediate layer and corresponding EDS elemental maps.

TaZrHfNbTi coating destroys its BCC structure and induces the formation of amorphous phases, although the underlying mechanism still requires further investigation.

3.2. Microscopic mechanical properties of the coating

The microhardness test results of the H13 steel substrate and the TaZrHfNbTi coating are provided in Table 2. The average Vickers microhardness of the TaZrHfNbTi coating is 967.64 $HV_{0.05}$.

Fig. 9 shows the nanoindentation load versus indentation depth curves of the H13 steel substrate and the TaZrHfNbTi coating. According to integral calculations, the elastic deformation work (W_e) and plastic deformation work (W_p) of H13 steel are 1.47×10^{-9} and 1.29×10^{-8} J, respectively, while those of the TaZrHfNbTi coating are 3.52×10^{-9} and 4.45×10^{-9} J, respectively. Under the same load, the plastic deformation work of the coating is only 34.5% of that of H13 steel, demonstrating good resistance to plastic deformation. In addition, the elastic deformation work of H13 steel and the TaZrHfNbTi coating accounts for 10.3% and 44.2% of their corresponding total work, respectively. This indicates that after deformation, the proportion of elastic deformation work stored in the coating to counteract the external force is much higher than that of the substrate, and the deformation recovery of the coating at the end of the applied force is also higher than that of the substrate. Hence, the TaZrHfNbTi coating exhibits a stronger load-bearing capacity.

The related mechanical properties of H13 steel and the TaZrHfNbTi coating are provided in Table 3. The maximum indentation depth of the TaZrHfNbTi coating is 440.63 nm, which is 40% lower than that of H13 steel, indicating a significant improvement in surface hardness. The calculated nano-hardness of the coating is 12.42 GPa. After unloading, the residual indentation depth of the coating is 254.77 nm, which is 61.39% lower than that of the substrate, further demonstrating that the TaZrHfNbTi alloy has good resistance to plastic deformation. The calculated elastic moduli of H13 steel and the TaZrHfNbTi coating are 258.82 and 208.27 GPa, respectively.

3.3. Melting loss behavior of the coating in dynamic molten aluminum at 680 °C

Fig. 10 presents the XRD patterns of the samples after dynamic corrosion in molten aluminum at 680 °C for 15 min, 40 min, 2 h, and 6 h. According to the XRD results, the corrosion products of H13 steel are mainly Fe_3O_4 and Fe_2O_3 [25]. As shown in Fig. 10(a), the oxide content increases continuously with corrosion time. Existing studies have shown that Fe—Al compounds, such as Fe_3Al and FeAl, are easily formed on the surface of steel in high-temperature molten aluminum due to the high affinity between Fe and Al [26]. However, in this study, no FeAl compounds were detected in the corrosion products of H13 steel. The FeAl compounds are highly brittle and prone to peeling off during the cleaning process of the corroded sample surface, so they were not detected. It is worth noting that even after corrosion for 6 h, neither iron oxides nor FeAl compounds were detected in the XRD patterns of the corroded coating samples, as shown in Fig. 10(b). This indicates that the coating did not peel off after corrosion at 680 °C for 6 h in dynamic

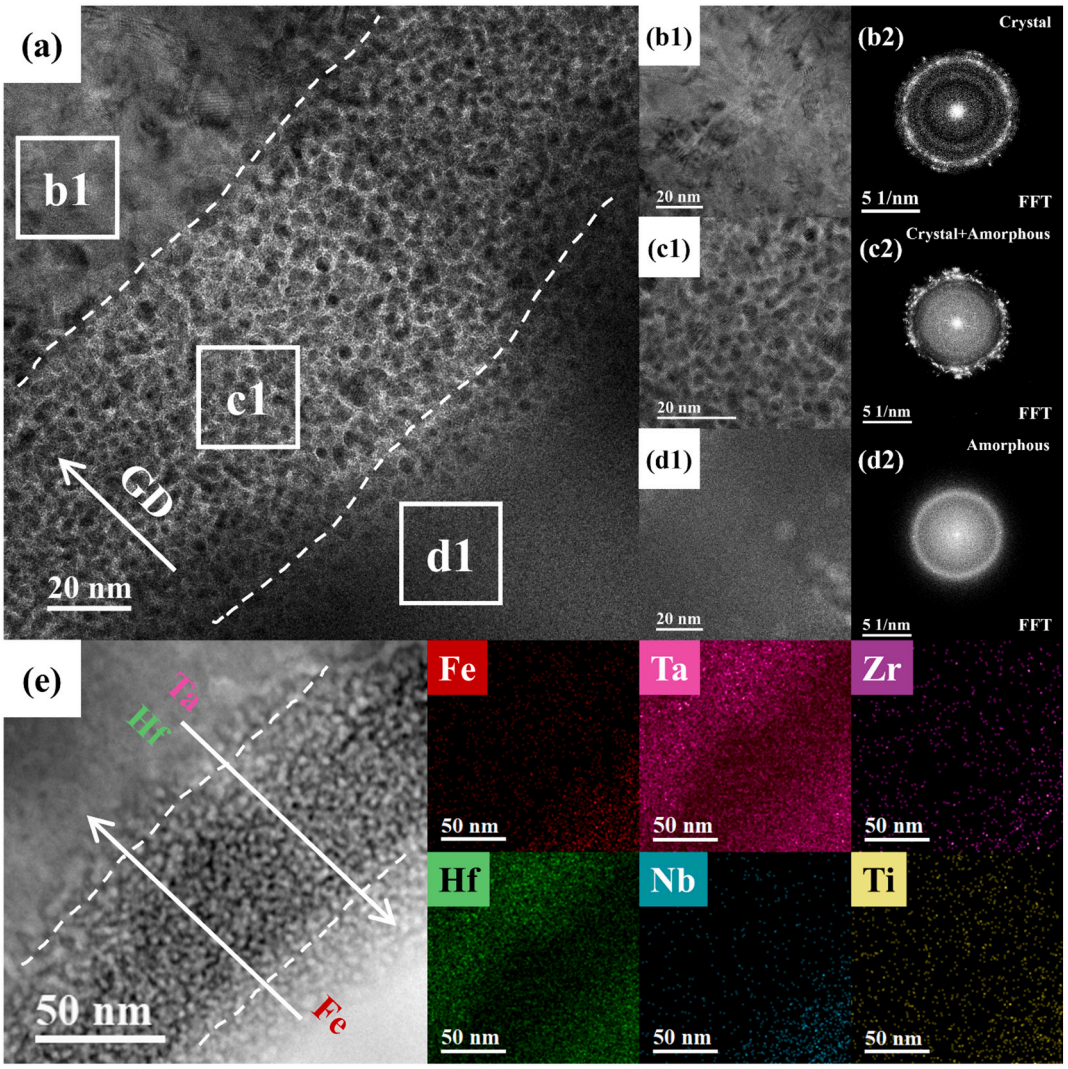

Fig. 8. Nanocomposite structure of the coating/matrix diffusion interface. (a) is the bright-field image of the coating/matrix diffusion interface. (b1), (c1) and (d1) are the local high-resolution bright-field images of the designated area in (a). (b2), (c2) and (d2) are the corresponding FFT patterns of (b1), (c1) and (d1). (e) HAADF-STEM image of coating/matrix diffusion interface and corresponding EDS elemental maps.

Table 2
Surface Vickers hardness of H13 steel and TaZrHfNbTi coating.

	Test point 1	Test point 2	Test point 3	Test point 4	Test point 5	Average
Substrate/ $HV_{0.05}$	525.62	504.32	540.74	507.69	483.56	512.39
Coating/ $HV_{0.05}$	1015.48	1029.67	900.23	877.34	1015.5	967.64

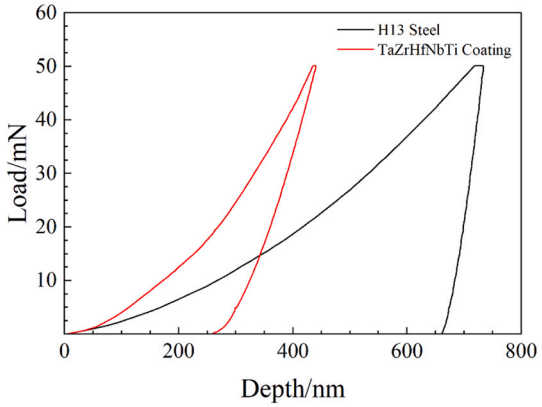

Fig. 9. Nanoindentation load versus indentation depth curves of H13 steel substrate and TaZrHfNbTi coating.

molten aluminum. In addition, the XRD results show that various phases appear on the surface of the remaining coating samples as the corrosion time increases. In the early stage of oxidation (15 min), Ti and Zr in the coating are first oxidized to form Ti_2O and ZrO_2 due to their high activity. With the extension of corrosion time, the BCC structure degrades due to the continuous oxidation and consumption of Ti and Zr, and some intermetallic compounds such as Al_3Ti, Al_2Ta, and HfNb appear in the coating under the corrosive effect of Al. Overall, the degradation of the HEA coating in dynamic molten aluminum starts with the oxidation of Ti and Zr, which have high oxygen affinity at elevated temperatures, leading to structural degradation of the BCC solid solution. Subsequently, Al_3Ti and Al_2Ta form due to the high affinity of Ti and Ta with Al, while the remaining Hf and Nb combine into HfNb. In the later stage of corrosion, Ta and Nb are also oxidized to TaO and NbO_2 under continuous high-temperature scouring and oxygen invasion. The XRD patterns of the coating after 6 h of corrosion were refined using the Rietveld method. The results indicate that the main corrosion products

Table 3
Nanoindentation test data of H13 steel and TaZrHfNbTi coating.

	H_{max}/nm	h_r/nm	H/GPa	E/GPa	H/E	H^3/E^2
Substrate	733.94	659.78	3.59	258.82	0.014	0.0007
Coating	440.63	254.77	12.42	208.27	0.059	0.0442

are ZrO_2, TaO, and $TiAl_3$, with weight fractions of 33.9 wt%, 31.2 wt%, and 23.6 wt%, respectively [27]. The fractions of $TaAl_2$ and HfNb were both below 10 wt%.

Fig. 11 shows the surface microscopic morphology of the coating samples after dynamic corrosion in molten aluminum at 680 °C for 15 min, 40 min, 2 h, and 6 h. In the early stage of corrosion, some oxides form on the coating surface, as shown in Fig. 11(a) and (b). Elemental analysis of regions (1) and (2) reveals that the main components of the oxide film are Ti, Zr, and O, consistent with the XRD results. With increasing corrosion time, the oxide film peels off, as shown in Fig. 11 (b). At 2 h of corrosion, significant degradation of the coating is observed, and "corrosion pits" begin to appear on the surface under the combined effects of molten aluminum and high-temperature oxidation. After 6 h, numerous corrosion pits with diameters of approximately 10 μm can be observed, indicating structural degradation of the coating surface layer.

Fig. 12 shows the cross-sectional microscopic morphology and corresponding EDS scanning results of the TaZrHfNbTi coating after dynamic corrosion in molten aluminum at 680 °C for different corrosion times. As shown, the corrosion film of the coating is mainly composed of oxides. However, after 6 h of corrosion in dynamic molten aluminum, the internal structure of the residual coating remains compact and intact. With increasing corrosion time, significant outward diffusion of Ti and Zr occurs due to their high oxygen affinity. Therefore, the continuous outward diffusion of Ti and Zr gradually induces degradation of the BCC structure in the coating. It is worth noting that slight outward diffusion of Fe is also observed at the bonding interface between the coating and substrate with increasing corrosion time. This indicates that the high temperature still induces minor mutual diffusion between the

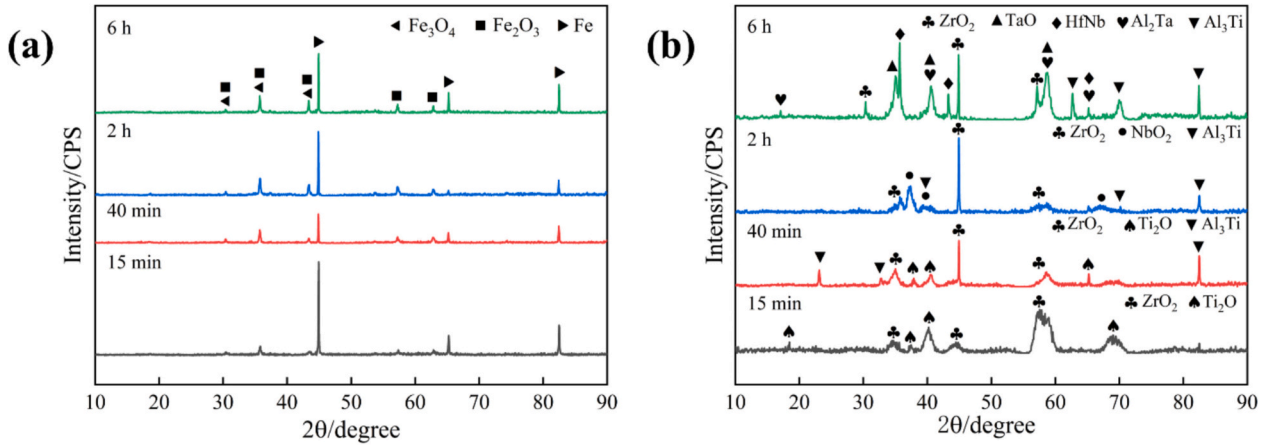

Fig. 10. Surface XRD patterns of the samples after dynamic corrosion in molten aluminum at 680 °C. (a) H13 steel. (b) TaZrHfNbTi coating.

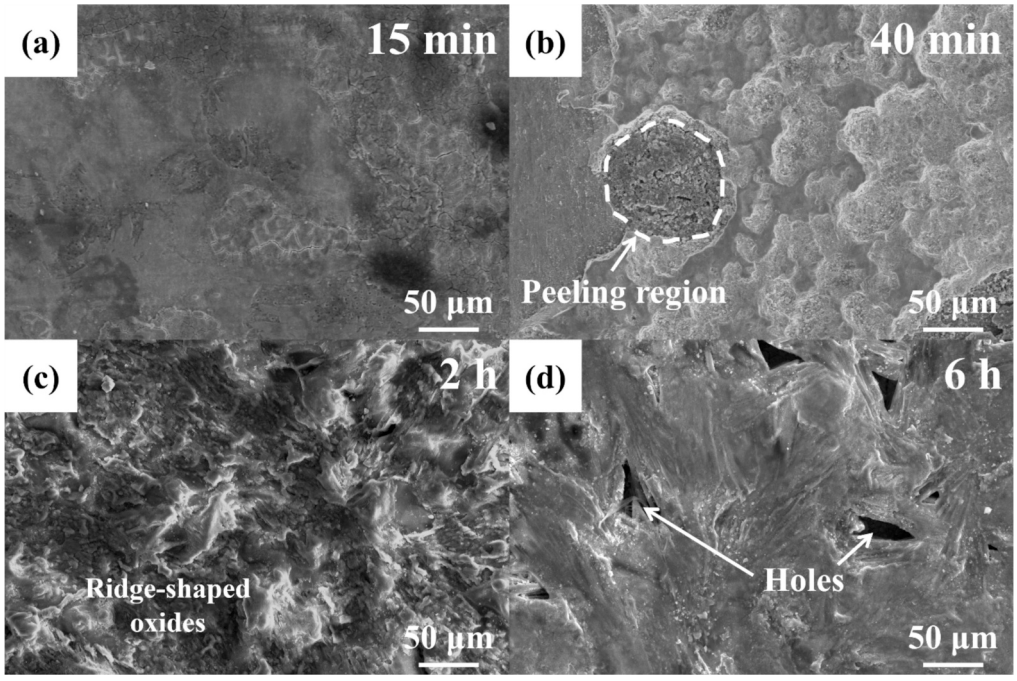

Fig. 11. Surface microscopic morphology of TaZrHfNbTi coating after dynamic corrosion in molten aluminum at 680 °C for different times: (a) 15 min, (b) 40 min, (c) 2 h, and (d) 6 h.

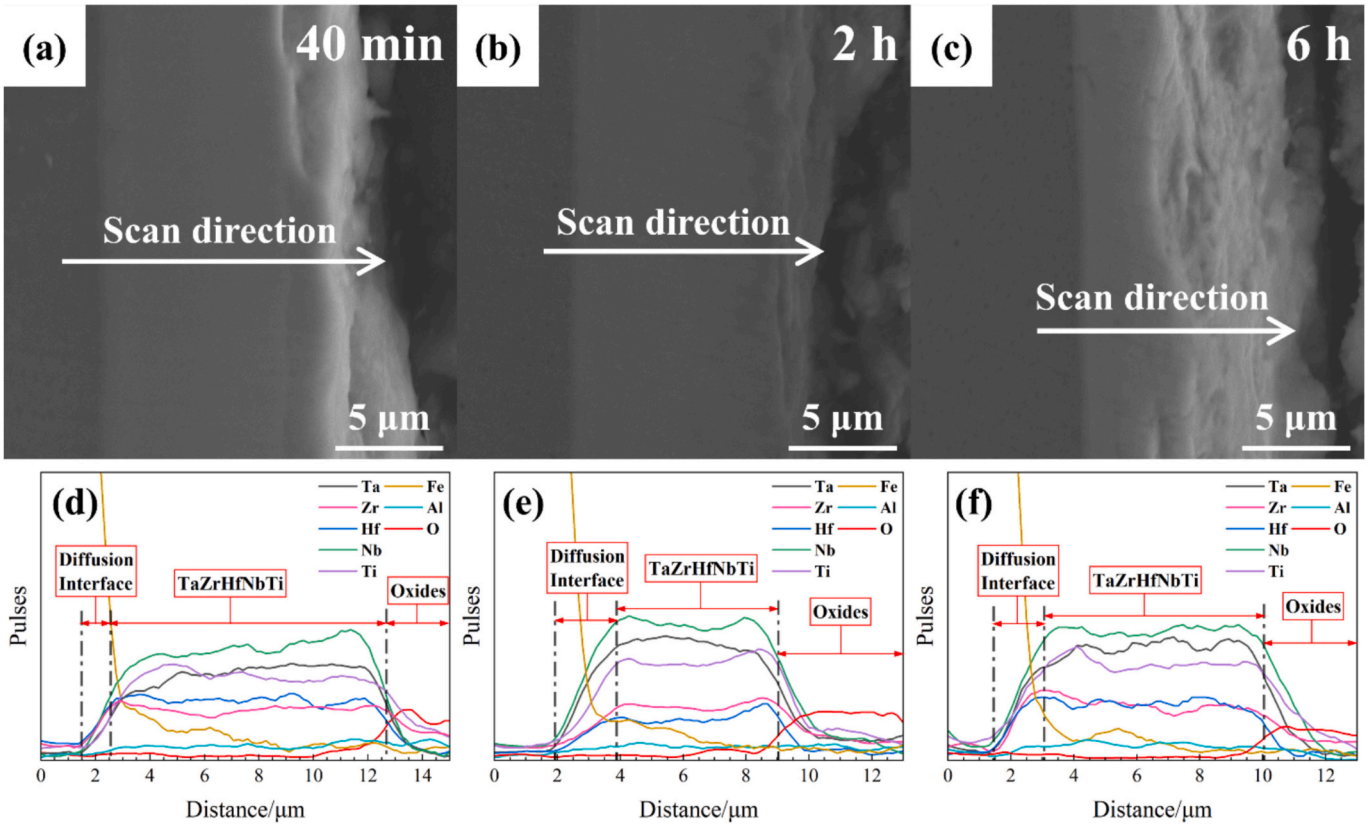

Fig. 12. Cross-sectional microscopic morphology and corresponding EDS scanning results of TaZrHfNbTi coating after dynamic corrosion in molten aluminum at 680 °C for different times: (a) 40 min, (b) 2 h, and (c) 6 h.

coating and substrate. These results demonstrate that the coating effectively hinders Fe diffusion from the substrate, thereby preventing the formation of destructive iron oxides and FeAl intermetallic compounds. The EDS profile reveals an increase in the Fe signal within the coated region. This phenomenon is attributed to back-sputtering that occurs during the deposition process, whereby a small number of Fe atomic clusters are ejected from the substrate. These sputtered Fe clusters are subsequently co-deposited onto the surface with the incoming high-entropy alloy clusters. This interpretation is consistent with the results from the depth-resolved TEM analysis of the coating.

Fig. 13 presents the surface three-dimensional morphology of the TaZrHfNbTi coating after corrosion in molten aluminum at 680 °C. With increasing corrosion time, the surface height difference increases, indicating deeper corrosion by molten aluminum, and the proportion of the surface area with significant melting loss gradually increases. For the corrosion area, the corrosion pit area of the coating in Fig. 13 was quantified, and the corrosion pit areas of the coating were 5.38%, 7.92% and 19.91% under the corrosion time of 40 min, 2 h and 6 h, respectively, which indicated that the corrosion pit area of the coating increased slowly [16]. On the contrary, the corrosion pit area of the substrate reached 36.78% only after 40 min minutes of corrosion. For the depth of corrosion, during the first 40 min of corrosion, no corrosion height difference is observed on the coating surface. After 6 h, the maximum corrosion depth of the TaZrHfNbTi coating is only 16.7% of that of the substrate.

Overall, the degradation mechanism of the coating was mainly attributed to the gradual degradation of the body-centered cubic (BCC) structure under high-temperature molten aluminum, during which each element in the coating either oxidized or formed intermetallic compounds, depending on its affinity with O and Al. Ti and Zr in the coating were oxidized to form Ti_2O and ZrO_2. Al_3Ti and Al_2Ta formed due to the high affinity of Ti and Ta with Al, while the remaining Hf and Nb combined into HfNb.

Fig. 14 shows the mass loss curve of TaZrHfNbTi coating after corrosion in molten aluminum at 680 °C. By linearly fitting the mass loss curve of the coating in Fig. 14, the following relationship is obtained: $\Delta m = -8.626 \times 10^{-4}\, t - 0.020$ ($R^2 = 0.9374$). Here, Δm is the mass loss in grams (g), and t is the time in minutes (min). The average melting loss rates of the substrate and the coating through calculation within 0 to 6 h are 7.19×10^{-2} and 2.15×10^{-2} g/(cm^2·h), respectively. The average melting loss rate of the coating is 70.1% lower than that of the substrate. These results indicate that the TaZrHfNbTi coating exhibits excellent corrosion resistance against dynamic molten aluminum.

As previously stated, under the influence of hollow cathode discharge-enhanced nonequilibrium sputtering, TaZrHfNbTi coating exhibited a gradient nanostructure and formed a diffusion bond with the substrate. It is noteworthy that the TaZrHfNbTi coating, characterized by its novel microstructure, exhibits significant interdiffusion with the substrate. This interdiffusion thereby provides a new approach for enhancing the coating-substrate adhesion of HEA coatings prepared by sputtering. It is foreseeable that this gradient-structured TaZrHfNbTi coating demonstrates potential for anti-corrosion applications in extreme environments involving multi-factor coupling. This study proposes an innovative strategy for designing and fabricating high-performance HEA coatings suitable for protection under extreme conditions where mechanical, thermal, and chemical factors are coupled.

4. Conclusion

This study prepared a TaZrHfNbTi coating with a gradient nanocomposite structure by hollow cathode discharge-enhanced plasma sputtering deposition. The coating's microstructure, microscopic mechanical properties and its melting loss behavior in dynamic molten aluminum were analyzed. The main findings and research results in this

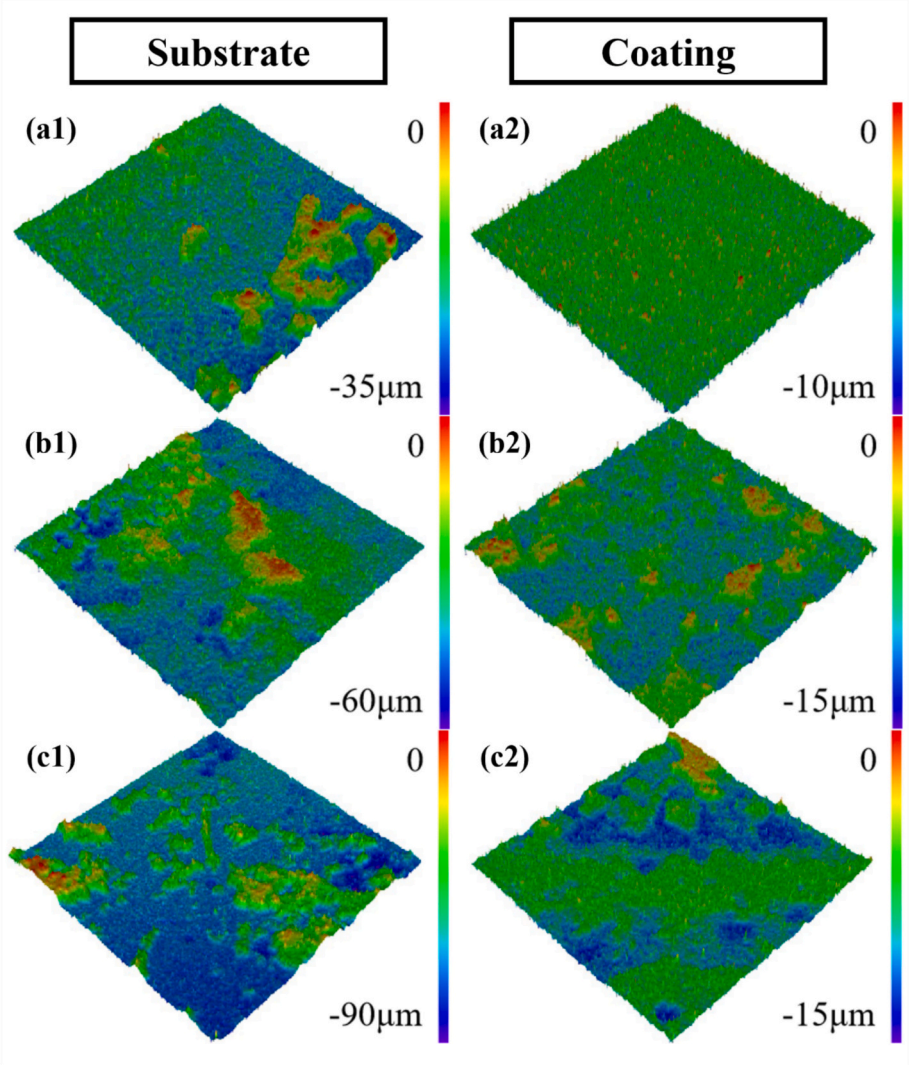

Fig. 13. Surface three-dimensional morphologies of H13 steel and TaZrHfNbTi coating after corrosion in molten aluminum at 680 °C for different times: (a) 40 min, (b) 2 h, and (c) 6 h.

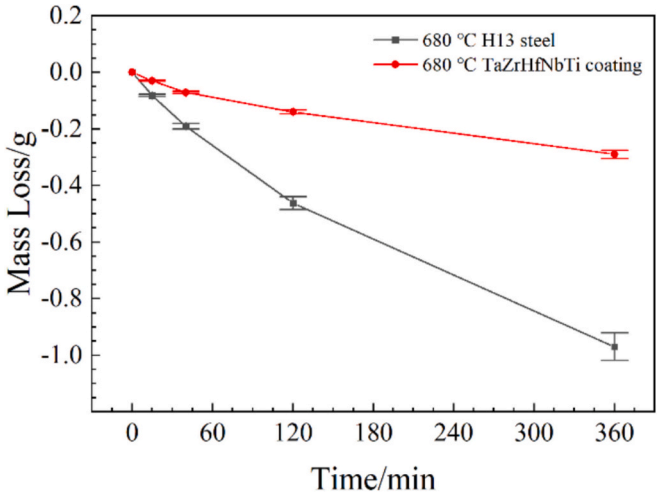

Fig. 14. Mass loss curves of H13 steel and TaZrHfNbTi coating during dynamic corrosion in molten aluminum at 680 °C.

paper are summarized as follows:

(1) A TaZrHfNbTi high-entropy coating with a diffusion interface and gradient nanostructure was successfully fabricated. The coating showed a characteristic "island bulge" morphology, exhibiting a uniform and dense structure with a thickness of approximately 19 μm.

(2) The coating exhibited a gradient nanostructure and formed a diffusion bond with the substrate. From the surface to the interior, the coating consisted of three different zones: a nanocomposite structure zone of "nanocrystalline + amorphous" in the outmost layer, a nanostructured columnar crystal zone in the intermediate layer, and a diffusion interface zone between the coating and the substrate. The coating demonstrated an average microhardness of 967.64 $HV_{0.05}$, a nano - hardness of 12.42 GPa, and an elastic modulus of 208.27 GPa.

(3) The coating did not peel off after corrosion at 680 °C for 6 h in dynamic molten aluminum. The primary degradation mechanism involved the destruction of the BCC structure in the molten aluminum at high temperature. Each element in the coating either oxidized or formed intermetallic compounds, depending on its affinity with O and Al. Additionally, the dynamic flow of molten aluminum accelerated the formation and spallation of surface oxides.

CRediT authorship contribution statement

Dongbo Wei: Writing – review & editing, Supervision, Resources, Funding acquisition. **Zuoxin Mao:** Writing – original draft, Validation, Methodology, Investigation. **Muyao Lin:** Visualization, Methodology, Formal analysis. **Pingze Zhang:** Supervision, Resources, Methodology. **Wenping Liang:** Supervision, Resources, Methodology. **Zhengjun Yao:** Supervision, Resources, Methodology. **Zhenyu Wang:** Supervision, Resources. **Aiying Wang:** Supervision, Resources.

Declaration of competing interest

The authors declare that they have no known competing financial interests or personal relationships that could have appeared to influence the work reported in this paper.

Acknowledgements

This work was supported by the National Key Research and Development Program of China (2024YFB3816500).

Data availability

No data was used for the research described in the article.

References

[1] X. Zhang, W. Chen, H. Luo, S. Li, T. Zhou, L. Shi, Corrosion resistance and interfacial morphologies of novel Fe-Cr-Mo-B cast steels in molten aluminum, Corros. Sci. 125 (2017) 20–28, https://doi.org/10.1016/j.corsci.2017.05.024.
[2] A. Persson, S. Hogmark, J. Bergström, Thermal fatigue cracking of surface engineered hot work tool steels, Surf. Coat. Technol. 191 (2005) 216–227, https://doi.org/10.1016/j.surfcoat.2004.04.053.
[3] W. Deng, S. Wang, T. Zhang, J. Zhang, Q. Zhai, C. Zhai, H. Zheng, Oxidation and failure mechanisms of CoCrFeNiMo HEA coatings at 1000 °C: insights into TGO evolution and interface diffusion, Surf. Coat. Technol. 509 (2025) 132229, https://doi.org/10.1016/j.surfcoat.2025.132229.
[4] H. Zhang, X. Zhang, J. Zhang, M. Pan, Vacuum plasma sprayed AlCoCrFeNi high-entropy alloy bond coating: vacuum heat-treatment, microstructure evolution and oxidation behavior analysis, Intermetallics 184 (2025) 108836, https://doi.org/10.1016/j.intermet.2025.108836.
[5] T. Zhao, L. Wang, S. Zhang, C.H. Zhang, X.Y. Sun, H.T. Chen, X.L. Bai, C.L. Wu, Effect of synergistic cavitation erosion-corrosion on cavitation damage of CoCrFeNiMn high entropy alloy layer by laser cladding, Surf. Coat. Technol. 472 (2023) 129940, https://doi.org/10.1016/j.surfcoat.2023.129940.
[6] F. Li, A. Chaurasiya, P. Zhang, D. Wei, B. Ouyang, R.S. Rawat, Y. Zhao, R. Tai, H. Jia, R. Liang, Microstructure and magnetic properties of CoCrCuFeNiTi high entropy alloy coatings based on plasma surface alloying technology, J. Alloys Compd. 1017 (2025) 179091, https://doi.org/10.1016/j.jallcom.2025.179091.
[7] R.D. Arnell, P.J. Kelly, Recent advances in magnetron sputtering, Surf. Coat. Technol. 112 (1999) 170–176, https://doi.org/10.1016/S0257-8972(98)00749-X.
[8] D. Wei, Z. Gao, X. Lv, J. Liu, P. Zhang, Study on the structure, growth pattern and corrosion behavior of CoCrFeNiAl high entropy alloy coatings - base on hollow cathode effect, Surf. Coat. Technol. 487 (2024) 130967, https://doi.org/10.1016/j.surfcoat.2024.130967.
[9] L. La, L. Wang, F. Liang, J. Zhang, G. Liang, Z. Wang, L. Qin, High-temperature oxidation and tribological behaviors of WTaVCr alloy coating prepared by double glow plasma surface alloying technology, Surf. Coat. Technol. 464 (2023) 129429, https://doi.org/10.1016/j.surfcoat.2023.129429.
[10] H. Yu, W. Liang, Q. Miao, T.L. Meng, M. Yin, N. Gong, R. Karyappa, X. Huang, X. Gao, Y. Song, A.C.Y. Ngo, H. Liu, Effect of C/N incorporation on structural and crystallographic properties of TaNbZr coatings deposited by double-glow plasma surface alloying on Ti-alloy substrate, Surf. Coat. Technol. 477 (2024) 130356, https://doi.org/10.1016/j.surfcoat.2023.130356.
[11] V. Nunes, F.J.G. Silva, M.F. Andrade, R. Alexandre, A.P.M. Baptista, Increasing the lifespan of high-pressure die cast molds subjected to severe wear, Surf. Coat. Technol. 332 (2017) 319–331, https://doi.org/10.1016/j.surfcoat.2017.05.098.
[12] Z. Xie, B. Liu, A. Fu, K. Li, Y. Cao, H. Zhou, J. Peng, Y. Liu, Combating Cl− and SO42−-induced molten salt corrosion by laser cladding FeCrNiMoAl high-entropy alloy coating, Surf. Coat. Technol. 494 (2024) 131429, https://doi.org/10.1016/j.surfcoat.2024.131429.
[13] Y. Garip, An investigation on the corrosion performance of Fe2CoCrNi0.5 based high entropy alloys, Corros. Sci. 206 (2022) 110497, https://doi.org/10.1016/j.corsci.2022.110497.
[14] X. Gong, T. Auger, W. Zhu, H. Lei, C. Xiang, Z. Yu, M.P. Short, P. Wang, Y. Yin, Intergranular precipitation-enhanced wetting and phase transformation in an Al0.4CoCrFeNi high-entropy alloy exposed to lead-bismuth eutectic, Corros. Sci. 196 (2022) 110038, https://doi.org/10.1016/j.corsci.2021.110038.
[15] X. Yang, Z. Fu, W. Chen, S. Li, H. Wang, S. Guo, E.J. Lavernia, Tribo-corrosion resistance of Ti-Nb-Cr-Mo-Al refractory high-entropy alloys in molten aluminum, Corros. Sci. 224 (2023) 111521, https://doi.org/10.1016/j.corsci.2023.111521.
[16] F. Ahmad, R.V. Babu, X. Kai, M.R. Abdullah, M. Hasan, S.M. Dar, A.W. Zia, Y. Zhao, L. Zhang, Oxygen concentration – a governing parameter for microstructural tailoring of duplex AlCrSiON coatings for superior mechanical, tribological, and anti-corrosion performance, J. Alloys Compd. 1002 (2024) 175345, https://doi.org/10.1016/j.jallcom.2024.175345.
[17] D. Liu, J. Lei, Z. Yan, Q. Zhang, Y. Du, C. Yang, B. Jiang, Study on the mechanism of aluminum melt corrosion of Fe-SG series metals, J. Mater. Res. Technol. 33 (2024) 6350–6362, https://doi.org/10.1016/j.jmrt.2024.11.033.
[18] R.R. Eleti, T. Bhattacharjee, A. Shibata, N. Tsuji, Unique deformation behavior and microstructure evolution in high temperature processing of HfNbTaTiZr refractory high entropy alloy, Acta Mater. 171 (2019) 132–145, https://doi.org/10.1016/j.actamat.2019.04.018.
[19] O.N. Senkov, J.M. Scott, S.V. Senkova, F. Meisenkothen, D.B. Miracle, C. F. Woodward, Microstructure and elevated temperature properties of a refractory TaNbHfZrTi alloy, J. Mater. Sci. 47 (2012) 4062–4074, https://doi.org/10.1007/s10853-012-6260-2.
[20] L. Zhao, M. Yi, C. Zhang, Y. Bai, Q. Guo, J. Zhang, H. Chen, G. Xiao, Z. Chen, C. Xu, Mechanical and wear properties of SiCw@Ni core-shell-reinforced (Hf,Nb,Ta,Ti,Zr)N high-entropy ceramic materials fabricated by spark plasma sintering, Tribol. Int. 214 (2026) 111384, https://doi.org/10.1016/j.triboint.2025.111384.
[21] C.T. Rueden, J. Schindelin, M.C. Hiner, B.E. DeZonia, A.E. Walter, E.T. Arena, K. W. Eliceiri, ImageJ2: ImageJ for the next generation of scientific image data, BMC Bioinformatics 18 (2017) 529, https://doi.org/10.1186/s12859-017-1934-z.
[22] D.Y. Kovalev, N.A. Kochetov, I.I. Chuev, Fabrication of high-entropy carbide (TiZrHfTaNb)C by high-energy ball milling, Ceram. Int. 47 (2021) 32626–32633, https://doi.org/10.1016/j.ceramint.2021.08.158.
[23] K. Xun, B. Zhang, Q. Wang, Z. Zhang, J. Ding, E. Ma, Local chemical inhomogeneities in TiZrNb-based refractory high-entropy alloys, J. Mater. Sci. Technol. 135 (2023) 221–230, https://doi.org/10.1016/j.jmst.2022.06.047.
[24] N. Wang, Q. Cao, X. Wang, S. Ding, D. Zhang, J.-Z. Jiang, Fluence- and thickness-dependent microstructure evolutions in Ti-Zr-Hf-Nb-Ta high entropy alloy thin films, J. Alloys Compd. 953 (2023) 170069, https://doi.org/10.1016/j.jallcom.2023.170069.
[25] G. Chen, L. Xue, J. Wang, Z. Tang, X. Li, H. Dong, Investigation of surface modifications for combating the molten aluminum corrosion of AISI H13 steel, Corros. Sci. 174 (2020) 108836, https://doi.org/10.1016/j.corsci.2020.108836.
[26] Q.Y. Zhang, Y. Zhou, J.Q. Liu, K.M. Chen, J.G. Mo, X.H. Cui, S.Q. Wang, Comparative research on dry sliding wear of hot-dip aluminized and uncoated AISI H13 steel, Wear 344–345 (2015) 22–31, https://doi.org/10.1016/j.wear.2015.10.017.
[27] B.H. Toby, R.B. Von Dreele, *GSAS-II*: the genesis of a modern open-source all purpose crystallography software package, J. Appl. Crystallogr. 46 (2013) 544–549, https://doi.org/10.1107/S0021889813003531.